Siderite dissolution coupled to iron oxyhydroxide precipitation in the presence of arsenic revealed by nanoscale imaging

1

2

3

4 *François Renard*[*,1,2], *Christine V. Putnis*[3,4], *German Montes-Hernandez*[2] *, and Helen E. King*[5]

5 [1]Department of Geosciences, Physics of Geological Processes, University of Oslo, Norway

6 [2]Univ. Grenoble Alpes, CNRS, ISTerre, CS 40700, F-38058, Grenoble cedex 9, France

7 [3]Institut für Mineralogie, University of Münster, Corrensstrasse 24, 48149 Münster, Germany

8 [4]The Institute for Geoscience Research (TIGeR), Department of Chemistry, Curtin University,

9 Perth, 6845, Australia

10 [5]Department of Earth Sciences, Utrecht University Budapestlaan 4, 3584 CD Utrecht, The

11 Netherlands

12

13 Corresponding author:

14 [*]François Renard

15 Department of Geosciences, PGP, University of Oslo, box 1048, 0316 Blindern, Oslo, Norway

16 francois.renard@geo.uio.no

Abstract

Siderite, the iron carbonate mineral, occurs in several geological environments and contributes to both the global iron and CO_2 cycles. Under crustal conditions, this mineral may dissolve, releasing iron that becomes oxidized and then precipitates in the form of iron oxides and oxyhydroxides that have a high affinity for pollutants, such as arsenic. The process of siderite dissolution, dissolved iron oxidation, and oxyhydroxide precipitation is coupled in time and space. Here, we study the entire process using time-lapse in-situ atomic force microscopy. Natural siderite crystals were dissolved at room temperature in acidic aqueous solutions in the presence or absence of arsenic. The dissolution process, whose rate could be measured at a nanometer scale, occurred by the nucleation and growth of etch pits, the retreat of step edges, and the deepening of cleavage steps. Precipitation of iron oxyhydroxide phases coupled to siderite dissolution was imaged in-situ. Nucleated particles have an initial height of 1-2 nm after 1 minute reaction and then grow with time into aggregate precipitates 130-220 nm wide and up to 80 nm high after 24 hours of reaction. Ex-situ stirred-flow reactor measurements confirm the same sequence of siderite dissolution and iron oxyhydroxide precipitation. The arsenic is adsorbed by iron oxyhydroxides and its presence does not change significantly the rate of dissolution-precipitation of the overall process. Results provide a basis for understanding and quantifying the interactions between reduced-iron minerals and aqueous-phase oxidants, as well as potential sequestration of toxic elements such as arsenic.

Highlights

- Siderite dissolution is coupled to iron oxyhydroxides precipitation in acidic conditions
- Siderite dissolution occurs by etch pits propagation, step retreat, and cleavage plane widening
- Arsenic is adsorbed by the precipitated iron oxyhydroxides

1. Introduction

Carbonates are common minerals in the Earth's upper crust and because of their high reactivity they dissolve and precipitate easily, thus playing a key role in the global cycle of carbon, controlling the weathering of continents and controlling the composition of groundwaters through pH, alkalinity or metal concentrations. Siderite, $FeCO_3$, is a trigonal carbonate mineral found in several geological environments, where it forms under reducing conditions providing sufficient iron in the 2+ oxidation state to build the mineral. It often occurs as a carbonate solid solution, with substitutions of the iron ion with Mg^{2+}, Mn^{2+}, Zn^{2+}, and a limited solid solution with Ca^{2+} (as a result of the ionic radii differences). It is also an end-product of bacterial anaerobic activity. In the presence of oxygen, Fe^{2+} from siderite is oxidized and thereafter participates in the global iron cycle through various $Fe^{(III)}$-rich oxides and oxyhydroxides.

1.1 Siderite in geological environments

Several studies show that siderite precipitates at shallow conditions and sometimes at depth during diagenesis (Morad et al., 1994; Milliken, 1998; Rossi et al., 2001; Stel, 2009). In some geological environments it is also found associated with the presence of arsenic. In all cases, siderite precipitation history is complex with successive events of siderite precipitation and dissolution largely controlled by the redox conditions. Rossi et al. (2001) described widespread siderite precipitation in sandstone reservoirs in the Khatatba formation in Egypt. There, siderite cements quartz grains and has produced a matrix strong enough such that compaction was reduced and porosity was preserved. Later dissolution of the siderite created a secondary porosity, enhancing reservoir properties of the rock. The siderite was assumed to have precipitated in shallow conditions, for example below swamps, where reducing conditions allowed the presence of Fe^{2+} in the pore water.

Carbonate cemented red-bed arkose deposits in the Central Iberian Chain (Spain) show that siderite participated in the formation and destruction of porosity during diagenesis (Stel, 2009).

67 In this example, reduction of iron oxides and the dissolution of calcite was followed by a

68 deformation episode during which the reducing fluid percolated along a nearby fault and caused

69 siderite precipitation. These reactions are associated with a volume loss close to 50% resulting

70 in secondary porosity.

71 Siderite limits iron aqueous concentration in geological environments and also its

72 bioavailability in soils and river and lake sediments. In acid mine drainage environments, it

73 represents a key component in the suite of mineral reactions that occur during reactive transport

74 in groundwaters (Walter et al., 1994). As Fe^{2+} is produced by the dissolution of sulfide minerals,

75 siderite can precipitate if limestone or dolomite dissolves nearby, saturating the fluid with

76 carbonate so that supersaturation with respect to siderite is reached. Numerical modelling shows

77 that once calcite is completely dissolved, siderite will also dissolve, releasing Fe^{2+} to the fluid

78 that can become oxidized and precipitate in the form of iron oxides and oxyhydroxides, such as

79 goethite (Walter et al., 1994). In the numerical simulations performed by these authors, a front

80 of siderite precipitates and then dissolves, moving with time in the same direction as the flow

81 of acid mine drainage.

82 In the Appalachian region, iron-contaminated groundwater leaks along abandoned and

83 unplugged oil and gas wells where siderite is the main source of iron into the water (Hedin et

84 al., 2007; Chapman et al., 2013). Strontium isotopes indicate that the enrichment in iron is due

85 to the downward percolation of acid water coming from surface spoils of coal mine products

86 through a siderite-rich shallow sandstone layer (Chapman et al., 2013), and then its upward

87 circulation along fluid pathways such as fractures and abandoned wells. Here, the mechanism

88 proposed is similar to that of acid mine drainage, where the siderite is the source of iron instead

89 of sulfide minerals. Siderite was also found in West Bengal sediments, where arsenic

90 contamination of groundwater is a major health issue (Pal et al., 2002). Finally the spatial

91 correlation of arsenic release and siderite dissolution was also observed at a local scale in the

92   groundwater contaminated by arsenic in the ChaiNan floodplain, Taiwan (Lin et al., 2006). As

93   proposed in the present study, a possible explanation of this observation is that arsenic is

94   adsorbed on iron oxyhydroxides that cover the siderite surfaces and is then released during

95   siderite dissolution because of pH variations.

1.2 Using siderite to remediate polluted waters

97   Siderite could be used in environmental technologies that remediate acid discharge pollution,

98   and several field and laboratory studies have provided data that characterize the coupled

99   processes involved. Processing the discharge of acidic effluents using reactive barriers is a

100 technology used to reduce the environmental impacts of acid mine drainage. The precipitation

101 of siderite is one of the many reactions that can buffer fluid pH and decrease iron concentration,

102 as observed in a field experiment near the Nickel Rim mine in Ontario (Benner et al., 2007). In

103 the case of soil contamination by arsenic, for example where As_2O_3 has been applied as a

104 herbicide, the use of siderite with an oxidizing agent could produce oxyhydroxides and trap

105 arsenic.

106 In laboratory conditions, a siderite/limestone reactor was proposed to trap arsenic and cadmium

107 from polluted water (Wang and Reardon, 2001). Fluids with high concentrations of iron,

108 cadmium, and arsenic were acidified with dissolved carbon dioxide and injected into a reactor

109 made of two successive columns. The first column contained siderite, which dissolved, released

110 Fe^{2+} that oxidized into Fe^{3+} and formed iron oxyhydroxides that could trap arsenic. Then, the

111 fluid was transported into a second column that contained calcium carbonate where cadmium

112 was trapped by the precipitation of calcium and cadmium carbonates. After some time the

113 efficiency of the first reactor was reduced and this was interpreted by an armoring effect of iron

114 oxyhydroxide coatings on siderite grains.

115 Guo et al. (2007a, 2007b) developed a water filtering technique that uses siderite as a natural

116 adsorbent of arsenic. In these studies, either 0.1-0.25 mm size siderite grains or mixture of

quartz, siderite, and hematite grains were reacted with arsenic contaminated water at concentrations in the range 0.2-1 ppm. Both $As^{(V)}$ and $As^{(III)}$ were successfully adsorbed. The proposed mechanism was an initial adsorption of arsenic on the siderite grains, and then the formation of iron oxyhydroxides (goethite or ferrihydrite) on which arsenic was later adsorbed or sequestered. Electron microscope images showed the formation of a 300 nm thick layer of iron oxides at the surface of the siderite grains (Guo et al., 2007a). Using X-ray photoelectron spectroscopy, it was confirmed that an iron hydroxide layer precipitated at the surface of siderite (Tang and Martin, 2011). All these studies show that dissolution of siderite and iron oxyhydroxide precipitation are coupled, and that iron oxyhydroxides can be used to sequester pollutants, such as arsenic.

Here, we perform in-situ time-resolved nanoscale imaging of the coupled process to document 1) the detailed mechanisms of siderite dissolution at low pH, in the range 1-5.5 and compare it with bulk dissolution experiments, 2) the precipitation rate and morphology of iron oxyhydroxide particles and how they nucleate and grow on the siderite surface, and 3) the possibility that arsenic is adsorbed during this process. The choice of low pH conditions in the range 1-5 is relevant for several environments such as leakage from oil and gas boreholes or acid mine drainage where arsenic and iron oxyhydroxides are observed (Benner et al., 1999; España et al., 2007) or even more extreme fluids with extremely low pH, as observed in an underground mine in California (Nordstrom et al., 2000). Our results complement previous studies where siderite dissolution was either measured in batch reactors (Golubev et al., 2009) or imaged using atomic force microscopy (Duckworth and Martin, 2004; Tang and Martin, 2011) and where adsorption of arsenic on iron oxyhydroxide was characterized (Dixit and Hering, 2003). These previous studies were limited in observing directly processes and measuring quantitative information on the rates of dissolution and precipitation at the nanoscale. Here, we observe that siderite dissolution occurs by three mechanisms at the atomic

142 scale: etch pits nucleation and spreading, step edge retreat, and widening and deepening of

143 cleavage planes. The present study also provides constraints on the mechanism of growth of the

144 iron oxyhydroxide particles and, for the first time, measure their size (height and width) as a

145 function of time. Because dissolution of siderite is coupled to precipitation of iron

146 oxyhydroxide, the whole process must occur in a boundary layer at the siderite surface.

147

148 **2. Materials and methods**

149 **2.1 Siderite crystals**

150 A siderite crystal (Einigkeit mine, Neunkirchen, Siegerland, Germany) was obtained from the

151 mineral collection of the University of Münster. Inductively coupled plasma - optical emission

152 spectroscopy (ICP-OES) revealed the composition of the crystal, with Mn (656 ppm or 6.86 wt.

153 %) and only trace amounts of Ca (46 ppm), Mg (147 ppm), Zn (421 ppb) and Sr (26 ppb)

154 detected. Fresh siderite fragments (ca. 4 x 2 x 1 mm) were prepared directly before each

155 experiment from this single siderite crystal by cleaving the crystal parallel to the {10-14} plane.

156 Several fragments were also crushed into powder for stirred flow-through reactor experiments.

157 **2.2 Solutions for siderite dissolution under the atomic force microscope**

158 Arsenic-free solutions and solutions with a controlled amount of arsenic ($As^{(III)}$ or $As^{(V)}$), with

159 the same ionic strength and various pH values, were used for siderite dissolution experiments

160 (Table 1). Several solutions with identical compositions were used to test the reproducibility of

161 the obtained results. Firstly, arsenic-free aqueous solutions with controlled pH, between 1.6 and

162 5.5, and ionic strength equal to 0.047 M were injected into a flow-through fluid cell of an atomic

163 force microscope (AFM) to dissolve the siderite surface. These solutions were prepared using

164 doubled deionized water (resistivity > 18 mΩ·cm) directly before each experiment. Sodium

165 chloride and hydrochloric acid were used to adjust ionic strength and pH, respectively. The pH

166 and salinity were adjusted according to thermodynamic simulations of equilibrated solutions

167   using the PHREEQC software (Parkhurst and Appelo, 1999). Then, solutions with $As^{(III)}$ or

168    $As^{(V)}$ oxyanions at concentrations of 50 or 500 ppm, with the same ionic strength as the arsenic-

169   free aqueous solutions initially used, were injected into the fluid cell, under several pH

170   conditions (Table 1). The arsenic solutions were prepared from salts of sodium arsenite

171   ($NaAsO_2$) and sodium arsenate dibasic heptahydrate ($Na_2HAsO_4 \cdot 7H_2O$) dissolved into double

172   deionized water. The pH of the solutions was controlled to be similar in the presence and in the

173   absence of arsenic. As well, the pH of all solutions was measured independently using a pH-

174   meter confirming the PHREEQC simulation results. All chemical agents were obtained from

175   Sigma Aldrich[®].

176   2.3 Atomic force microscopy imaging

177   The siderite surfaces were scanned at room temperature (23±1 °C) using a Bruker Multimode

178   Atomic Force Microscope (AFM) operating in contact mode. All time-resolved sequences were

179   acquired downscan. The experiments were performed in-situ within an O-ring sealed flow-

180   through fluid cell from Digital Instruments (Bruker). Volumes of 2 mL of solutions were

181   injected with a syringe between each scan, at regular time intervals of approximately 1.5

182   minutes, giving an effective flow rate of 22 $\mu L \cdot s^{-1}$. This flow rate ensures that processes

183   occurring at the mineral surface are reaction-controlled, rather than diffusion controlled (Ruiz-

184   Agudo et al., 2010).

185   AFM images were collected using Si_3N_4 tips (Veeco Instruments, tip model NP-S20) with

186   spring constants 0.12 N m^{-1} and 0.58 N m^{-1}. Images were analyzed using the NanoScope

187   Analysis software (Version 1.5). At the beginning of each dissolution experiment, deionized

188   water was injected over the siderite surface for several minutes, to observe any reaction or

189   dissolution. For several samples, the dissolution was followed under the AFM for several hours,

190   then the sample was removed from the flow cell, left in contact with the solution for 12 to 20

191   hours, and then imaged again, to allow sufficient time for reaction.

2.4 Ex-situ dissolution experiments

Ex-situ siderite dissolution stirred flow-through reactor experiments were performed to determine if arsenic is adsorbed on siderite. Two flow-through reactors of 50ml (internal volume) were firstly filled with high-purity water, one reactor containing 1g of natural siderite ground in a McCrone micronizer agate mortar in ethanol for 8 minutes (particle size < 30 μm). The other reactor did not contain siderite and was used passively to trace the fluid and show that no adsorption occurred on the walls. Then, an arsenic-rich solution (100 to 500mg/L of As$^{(III)}$ at pH=5 or 100 to 500mg/L of As$^{(V)}$ at pH=2) was percolated in both reactors using a constant flow rate of 3.3 ml/minute. The siderite-solution suspension in the reactor was continuously stirred by a magnetic Teflon bar at room temperature (20°C). The outflow solutions were filtered in-situ through 0.2μm pore size Teflon membranes (located on the top of reactors) and pH and ICP-AES (inductively coupled plasma - atomic emission spectroscopy) analyses were taken on-line. Thereby iron and arsenic concentrations were measured as a function of time allowing to detect i) if iron is released in the fluid, ii) if arsenic is adsorbed onto siderite or the produced iron oxyhydroxides.

2.5 Raman spectroscopy

A confocal Raman spectrometer (WITec Alpha 300R) operating with the 532 nm line of a Nd-YAG laser was used for analysis of reaction products. Samples with large numbers of precipitates observed in the AFM experiments and the powders from the reactor experiments were selected for Raman investigations. The original siderite was also analyzed as a reference. To survey samples for newly precipitated material, different areas of the sample surface with visual precipitates were scanned using the continuous scan mode with an integration time of 0.2 s. A filter averaged over 2x2 pixels was used to identify areas of the spectra where additional, weaker peaks unrelated to the underlying siderite were present. Once an area with additional peaks was detected a depth scan was used with the same parameters as the continuous

217 scan to determine the best focal point. Finally, a single spectrum with improved signal to noise

218 ratio was obtained using an integration time of 5 s and integrated 50 times. All spectra were

219 obtained using a grating of 1800 grooves/mm and a pinhole of 20 µm. Spectral background

220 removal and peak fitting was conducted using the WITec Project Plus software.

221

222 **3. Results**

223 **3.1 In-situ atomic force microscope experiments**

224 The siderite cleaved surface is characterized by the presence of steps (Figure 1a). Direct in situ

225 observations showed that in contact with acidic solutions, the siderite surface starts dissolving

226 along steps that retreat, through the formation and propagation of etch pits with typical

227 rhombohedral shapes (Figure 1b), and through the deepening and widening of step edges along

228 cleavage planes (Figure 1c). Etch pit steps were typically one unit cell (4.72 Å) high, before

229 deepening. A high nucleation rate of small etch pits over the reactive surface was observed and

230 these pits spread sideways to merge and remove successive unit-cell heights layer by layer. The

231 dissolution rate v_{diss_pit} was measured from etch pit spreading (see Ruiz-Agudo and Putnis

232 (2012) for details of measurements and etch pit growth in Figure 1d). Some deeper pits also

233 formed as rows along the surface, probably indicating the position of defects or ion

234 substitutions. Dissolution along steps of cleavage directions was also frequently observed. In

235 one case, the direct dissolution rate could be measured as the dissolution along a cleavage step

236 was followed for 115 minutes (see profile in Figure 1c). The widening and deepening of the

237 step was characterized (Figure 2) and showed non-linear time evolution. Note that the ratio

238 between width and depth of the steps remained constant (linear trend in Figure 2d), indicating

239 that dissolution occurred by the removal of the constituent ionic species perpendicular to the

240 surface. The rate of siderite dissolution normal to the surface (Figure 2a), was measured equal

241 to $v_{diss\_cleav}=0.005\pm0.002$ nm·s^{-1}, for this example where pH was 2.1 and temperature was 23°C.

242 Taking the molar volume V_m of siderite into account (29.43 $cm^3 \cdot mol^{-1}$), a local kinetics constant

243 can be calculated as $k_{loc} = v_{diss\_cleav}/V_m$ and is in the range $1.7 \cdot 10^{-7} \pm 0.7 \cdot 10^{-8}$ $mol \cdot m^{-2} \cdot s^{-1}$, and

244 $\log_{10}(k_{loc}) = -6.8$. This value is very close to the value $\log_{10}(k) = -6.5$ measured by Duckworth

245 and Martin (2004) using batch reactor experiments and representing a dissolution rate averaged

246 over a large number of grains. At pH 1, the rate of etch pit propagation could be measured

247 (Figure 1d) and found to be $v_{diss\_pit} = 0.14 \pm 0.05$ $nm \cdot s^{-1}$. This dissolution was very localized,

248 therefore an average dissolution rate could be calculated only if the density of these etch pits

249 over the whole surface of the sample could have been estimated, which is not the case here.

250 The precipitates initially formed as small spots, with an average size of a few nanometers

251 (Figure 3a,b), distributed more or less randomly on the siderite surface and showed low

252 adhesion, as they were easily moved by the AFM tip at the initial stage of precipitation. With

253 time, they tend to localize near step edges (Figure 3c) or near deep etch pits (Figure 3d) or,

254 close to locations where dissolution was more intense. This means that dissolution sites, where

255 more iron was released, control the nucleation process of ferric precipitates. Then, these

256 precipitates grew in size into larger rounded structured aggregates, probably growing by an

257 aggregation process, as already observed using high resolution TEM and X-ray microscopy

258 imaging of several iron oxyhydroxides produced in micro-reactors (Abou-Hassan et al., 2009;

259 Byelov et al., 2013), see Figure 3e. After leaving the sample overnight, these precipitates

260 covered the entire surface of the siderite (Figure 3f) and showed preferential alignment along

261 steps.

262 The shape and size of these precipitates can be measured in all experiments where they were

263 observed (Figure 4) and all showed that they formed patches with a more or less circular

264 perimeter, a low height to diameter aspect ratio, and no evidence of crystallographic facets.

265 Images were collected at different times, under different conditions, and over differing areas of

266 observation. Also scanning was performed in different directions. Under all these conditions

267 the precipitated particles we observed presented rounded perimeters. At the scale of our AFM

268 observations tip-shaped convolutions would therefore be minimal and we conclude that the

269 circular shapes measured is representative of the precipitate particles.

270 The diameter of the precipitates measured for one experiment at pH 2.1 at three different times

271 (0.1, 1, 23 hours) show mean values in the range 130-220 nm with standard deviation of ±60nm

272 (Figure 4b). This quite large standard deviation does not allow us to determine whether the

273 average precipitate diameter increases or decreases with time, and on average, within the

274 deviation, it appears to remain constant. The heights of the precipitate particles tend to increase

275 with time (Figure 4c), reaching up to 80 nanometers after 24 hours. The trend for the height

276 increase with time is robust with a constant linear growth velocity of 0.012 nm/s (Figure 4d),

277 higher than the values in the range 0.0001-0.0006 nm/s measured by Weidler et al. (1998) for

278 the growth of goethite, at pH close to 5 and probably different supersaturation, however.

279 To summarize, the coupled dissolution-precipitation process involves the dissolution of the

280 siderite substrate, releasing $Fe^{(II)}$, and the nucleation of precipitates that grew in diameter until

281 they reached a size in the range 130-220 nm, and then grew in height to 10-80 nanometers. With

282 time the siderite surface became covered by these particles that produced several layers of

283 precipitates (Figure 3f). There is therefore a balance between nucleation of new precipitates and

284 growth of existing ones. Their rounded shape probably indicates low crystallinity or possibly

285 an amorphous phase. These observations are seen for very acidic to low acidic fluids, whether

286 or not arsenic is present. For the two experiments at high pH (experiments sid13 and sid14 in

287 Table 1), no evidence of dissolution was observed and no precipitates could be observed,

288 probably because the kinetics was slower and could not be captured during the course of an

289 AFM experiment (averaging several hours).

290 The surface dissolution-precipitation reactions, including iron oxidation at the siderite surface

291 can be written as follows:

292    $\equiv FeCO_3 + H^+ \rightarrow Fe^{2+} + HCO_3^-$ (dissolution process)

293    $Fe^{2+} + HCO_3^- + 0.5O_2 + 1e \rightarrow FeOOH + CO_2$ (iron   oxidation   and   oxyhydroxide

294   precipitation)

295   Here, we assume the most common iron oxyhydroxide group (goethite, lepidocrocite, and

296   akaganeite) in oxidant systems.

297   **3.2 Ex-situ experiments**

298   The stirred flow-through reactor experiments (see Section 2.4) showed an initial increase of

299   iron concentration in the fluid collected at the outlet, and demonstrated siderite dissolution

300   (Figure 5). After about 100 minutes, the concentration of iron in the fluid tends to decrease,

301   which is interpreted by the precipitation of iron oxyhydroxides. Despite the high amount of

302   arsenic used in these experiments, no clear adsorption could be observed. This is due to the fact

303   that arsenic adsorbs more preferentially on iron oxyhydroxide rather than onto siderite and the

304   rate of iron oxyhydroxide production was slow when considering the experimental durations

305   used here. Scanning electron microscopy images showed the precipitation of iron oxyhydroxide

306   on siderite (Figure 5f). The stirred-flow reactor experiments therefore confirm what was

307   observed in-situ by AFM, that is, a coupled dissolution-precipitation process where the iron

308   produced by siderite dissolution was oxidized forming particles of iron oxyhydroxide

309   precipitates.

310   **3.3 Raman measurements**

311   Coupled to dissolution, precipitates formed on the siderite surface (Figure 3). The precipitated

312   particles were generally too small and reacted with the Raman laser beam thus making them

313   difficult to analyze using Raman spectroscopy. After experiments in the flow-through reactor,

314   the solid reaction product was also analyzed using Raman spectroscopy (Figure 6).

315   A broad Raman peak was observed at 857 cm^{-1} after the reactor experiments at pH 5 (spectrum

316   D in Figure 6). This is consistent in position with the observed double peak produced during

317   arsenic adsorption to amorphous Fe-oxides in pH 5 solutions (Goldberg and Johnson, 2001). A

318   slight shoulder is also observed at lower wavenumbers on the siderite related peak at ~730 cm^{-}

319   ^{1} indicating the presence of an iron-phase such as ferrihydrite, which produces a weak broad

320   band in this region (Hanesch, 2009). A weak broad peak in the same position was also observed

321   after the pH 2 reactor experiments along with a second phase that produced more intense peaks

322   at 244, 370, 640 cm^{-1}. This is similar to goethite, although at lower wavenumbers than those

323   reported previously (Hanesch, 2009). In addition, the spectra indicate that a hydrated Fe-

324   arsenate phase forms in these experiments.

325   The AFM experiment sid10 (pH 5.5, no arsenic, see Table 1) showed precipitates with peaks at

326   242, 393 and 637 cm^{-1}. The orange color of the precipitates visible under the light microscope

327   of the Raman spectrometer and the similarity of the peak positions to other Fe-oxyhydroxide

328   phases (Hanesch, 2009) as well as the expected formation of akaganeite and goethite under the

329   experimental conditions, indicates that the precipitates are probably an iron-oxyhydroxide

330   phase. To conclude, both SEM imaging coupled to EDS (Figure 5f) and Raman spectroscopy

331   (Figure 6) performed on flow-through reaction products and one sample used for AFM

332   experiments indicate that the precipitates are oxyhydroxides (goethite, ferrihydrite). In some

333   cases, the existence of an As-Fe phase is detected by a weak Raman peak (spectrum D in Figure

334   6). However, it cannot be a major phase in the system studied here.

335

336   **4. Discussion**

337   In the experiments, the pH of the injection solution is fixed whereas the Eh potential

338   is not controlled. In both AFM flow cell and flow-through reactors, the injected fluid

339   is in equilibrium with atmospheric oxygen, and the conditions are oxic. If one

340   considers the pH/Eh diagram of iron in water (Beverskog and Puigdomenech, 1996),

341   the experimental conditions are near the end of the stability field for Fe(OH)$_3$ where

342   high quite Eh is needed to precipitate oxyhydroxide. Further, if one overlaps the

343   Eh/pH stability field of arsenic (Lu and Zhu, 2011) on top of the Fe-H_2O system

344   diagram, arsenic is soluble in the experimental conditions. These two Eh/pH

345   diagrams are represented on the Figure 7. The experiments were likely saturated by

346   atmospheric oxygen, but given the isolated set-up of AFM fluid cell, there is a

347   possibility that the Eh could drop quickly when siderite dissolves to release ferrous

348   ion. In this case, arsenic adsorption will be less significant. However, in cases where

349   iron oxyhydroxide precipitates are widespread, arsenic can adsorb on these phases

350   and be removed from the solution.

351   **4.1 Dissolution of siderite**

352   Carbonate minerals dissolve with a rate that decreases from calcite to dolomite, siderite, and

353   magnesite. The dissolution reaction of siderite under conditions relevant for natural

354   environments, such as bottoms of lakes or geological reservoirs, was measured in several

355   studies (Singer and Stumm, 1970; Reiterer et al., 1981; Bruno et al., 1992; Duckworth and

356   Martin, 2004; Tang and Martin, 2011). Siderite dissolves in water according to the reaction

357     $FeCO_{3(s)} + 2H^+ \rightarrow H_2O + CO_{2(g)} + Fe^{2+}$, with an equilibrium constant K_0 equal to $10^{-7.59}$ at 25°C,

358   under neutral pH conditions and in a 1M $NaClO_4$ solution (Bruno et al., 1992). At pH below

359   6.5, room temperature, and in the absence of oxygen, the iron remains in the form of dissolved

360   Fe^{2+} in the fluid, whereas at pH above this limit, ligands form in the fluid such as $FeCO_{3(aq)}$ up

361   to pH 8.5 and $Fe(CO_3)_2^{2-}$ above 8.5 (Bruno et al., 1992). The kinetics of dissolution at 25°C and

362   in oxic and anoxic conditions is constant at pH in the range 5.5-10 and increases by decreasing

363   the pH below 5.5 (Duckworth and Martin, 2004).

364   Atomic force microscopy images show that dissolution occurs by the formation and extension

365   of rhombohedral etch pits, sometimes aligned along cleavage or fracture planes, and retreating

366   of step edges (Duckworth and Martin, 2004; Tang and Martin, 2011). This is consistent with

367 other carbonate mineral dissolution (see Ruiz-Agudo and Putnis (2012) for a review of AFM

368 measurements and observations). Duckworth and Martin (2004) observed that the shape of

369 rhombohedral etch pits with an initial obtuse angle of 102° evolved during dissolution and the

370 obtuse angle decreased to 72° after 4 hours. Tang and Martin (2011) observed alignments of

371 etch pits along fractures and dissolution by step edge retreat. Here, we show that a

372 complementary mechanism, the widening and deepening of cleavage steps is also involved in

373 siderite dissolution. When observing the dissolution of cleavage steps in AFM, their widening

374 gives access to the rate in a plane perpendicular to the dissolving interface, whereas etch pits

375 are usually interpreted as showing the rate of dissolution of atoms in the plane of the interface.

376 Our data show that dissolution occurs at the mineral-water interface in-plane (by etch pit lateral

377 propagation) and in a perpendicular direction (by etch pit deepening or dissolution at cleavage

378 steps). Moreover, we provide dissolution rates at the microscopic scale, $v_{diss\_pit} = 0.14 \pm 0.05$

379 $nm \cdot s^{-1}$ for the spreading of etch pits at pH 1 and $v_{diss\_cleav} = 0.005 \pm 0.002$ $nm \cdot s^{-1}$ for the widening

380 of cleavage at pH 2.1.

381 Golubev et al. (2009) studied the kinetics of siderite dissolution in batch reactor experiments,

382 at pH in the range 1 to 4.6 and partial pressure of CO_2 in the range 10^5-$5 \cdot 10^6$ Pa. They showed

383 that the siderite dissolution rate decreases with increasing pH in the range 1-4.5, and increases

384 with temperature with an activation energy in the range 48-61 $kJ \cdot mol^{-1}$, depending on pH and a

385 negligible effect of the partial pressure of CO_2. The dissolution rate of siderite was measured

386 on powder at 25°C close to $10^{-6.5}$ $mol \cdot m^{-2} \cdot s^{-1}$ at pH 1.5 and decreases to $10^{-8.65}$ $mol \cdot m^{-2} \cdot s^{-1}$ as pH

387 increases to 6, as seen in the figure 2 in Duckworth and Martin (2004). A slightly higher value

388 was obtained by Golubev et al. (2009) when using a rotating disk apparatus, with a dissolution

389 rate decreasing from $10^{-5.2}$ to 10^{-6} $mol \cdot m^{-2} \cdot s^{-1}$ while the pH increases from 1 to 3. A value of $10^{-6.5}$

390 $mol \cdot m^{-2} \cdot s^{-1}$ at pH 2 was obtained by Tang and Martin (2011), which then decreases as pH

391 increases. All these values measured with different techniques and by different groups point to

392 the same value, similar to what we measured on the lateral widening of a cleavage step (Figure

393 2) and indicating that the dissolution rate at a local scale is similar to that of the bulk.

394 **4.2 Iron oxyhydroxide precipitation in a boundary solution layer**

395 The dissolution of siderite may be more complex because it is coupled to the precipitation of

396 iron oxyhydroxides that would then tend to passivate siderite surfaces, reducing dissolution. At

397 pH below 10.3, a mechanism of coupled dissolution and precipitation has been proposed that

398 involves four successive steps: 1) the release of Fe^{2+} by siderite dissolution, 2) the formation of

399 a $(Fe^{2+}OH)^+$ complex that reacts with O_2 present in the fluid, 3) the formation of an aqueous

400 complex $(Fe^{3+}(OH^-)_3)^0$, and 4) the precipitation of solid $Fe^{III}(OH)_3$ (Duckworth and Martin,

401 2004; Tang and Martin, 2011). The precipitation of an $Fe^{(III)}$ oxyhydroxide layer may cover the

402 siderite surface (Guo et al., 2007a; Tang and Martin, 2011), passivate it, and significantly

403 modify dissolution rates. We directly observe this effect during in-situ experiments where iron

404 oxyhydroxides precipitate on the siderite surface and cover it in less than 24 hours for the low

405 pH solutions. Here, we show as well that the oxyhydroxides nucleate or arrive at the surface as

406 tiny nm size particles and then initially grow as probably non-crystalline rounded (amorphous)

407 particles, 130-250 nm wide and up to 80 nm height. They accumulate on the siderite surface

408 and could produce several successive layers, decreasing the surface area available for further

409 dissolution.

410 Davison and Seed (1983) measured the kinetics of oxidation of $Fe^{(II)}$ into $Fe^{(III)}$ in natural

411 freshwaters and the laboratory in the neutral pH range and fitted the following kinetic

412 relationship:

413
$$-\frac{d[Fe^{(II)}]}{dt} = k[Fe^{(II)}]pO_2[OH^-]^2 = k_1[Fe^{(II)}]$$

414 where k is the rate constant, pO_2 is the partial pressure of oxygen, $[OH^-]$ represents the effect

415 of pH, and k_1 is a rate constant where the effects of oxygen and pH are embedded together. At

416 room temperature, partial pressure of oxygen close to atmospheric and pH close to neutral, the

417 value of k is close to $2 \cdot 10^{13}$ mol$^{-2} \cdot$l$^2 \cdot$atm$^{-1} \cdot$min^{-1} and the half time of the reaction is in the range

418 1-6 hours. Applied to the present experiments, the time scale of Fe$^{(II)}$ oxidation is therefore

419 larger than the time scale of the whole dissolution-precipitation process we observe. This

420 implies that the oxidation of Fe$^{(II)}$ could be the limiting step of the whole dissolution-

421 precipitation process. It also implies that because the time scale for the whole process measured

422 in the AFM experiments is shorter than what Davison and Seed (1983) measured for the

423 oxidation of Fe$^{(II)}$, either the access of oxygen in our experiments is easier than in their

424 experiments, or the presence of siderite and/or goethite helps to catalyze this oxidation reaction,

425 as already proposed in other studies (Weidler, 1998; Liu et al., 2007).

426 The growth of goethite crystals was studied using atomic force microscopy at room temperature

427 and pH 4.85 (Weidler et al., 1998). Results show that (100) and (110) faces of goethite grow at

428 velocities in the range $1-6 \cdot 10^{-4}$ nm$\cdot$s^{-1}, which is one to two orders of magnitude slower than

429 what we measured in our AFM experiments for the growth in height of the oxyhydroxide

430 particles at pH 2.1 (Figure 4d). The difference between the rate they measured at pH 4.85 and

431 the rate measured in the present study at pH 2.1 could be related to the fact that dissolution of

432 siderite is two orders of magnitude faster at pH 2.1 than at pH 4.85, releasing much more iron

433 in solution, and increasing the local supersaturation with respect to goethite near the surface.

434 Weidler et al. (1998) calculated that the rate of Fe$^{(III)}$ complexation at the goethite surface was

435 one to two orders of magnitude larger than in the bulk solution, and that therefore goethite

436 catalyzed this transformation. In addition, the presence of trace amount of Fe$^{(II)}$ adsorbed on

437 ferrihydrite can catalyze its transformation into goethite, even at room temperature (Liu et al.,

438 2007).

439 Two models for precipitation of iron oxides can be proposed: 1) the homogeneous nucleation

440 in the fluid by oxidation of Fe$^{(II)}$, or 2) the heterogeneous nucleation at siderite or iron

441 oxyhydroxide surfaces. Our data show that the iron oxyhydroxides precipitate directly on the

442   siderite surface, favoring the heterogeneous nucleation model. As mentioned previously, the

443   nucleated nanoparticles grew by aggregation of primary nanoparticles, then leading to rounded

444   structured aggregates similar to mesocrystals if crystalline nanoparticles are involved (Montes-

445   Hernandez et al., 2015); however, from AFM observations it is difficult to obtain information

446   on the crystallinity of precipitating particles. The subsequent coalescence of nanometer size

447   particles to form larger single crystals has been reported for the growth of both calcite and barite

448   (Gebauer et al., 2008; Ruiz-Agudo et al., 2015) and has contributed to the current debate about

449   non-classical crystal growth mechanisms (Teng, 2013).

450   From the AFM observations, the first particles (a few nm in size) were present on the siderite

451   surface immediately within the first second of scanning and appeared to come directly from

452   solution as opposed to nucleating on the surface. Then after successive scans (each scan lasted

453   65-70 s) the small nanometer sized particles could be seen to increase in size by coalescence

454   with adjacent particles (Figure 3e-f).

455   The solubility product $K_{s,0}$ of $Fe^{(III)}$ oxyhydroxide equilibrium in aqueous solution follows the

456   relationship $K_{s,O} = a_{Fe(III)}(a_{OH-})^3$ at 25°C and shows cubic pH dependence. The value of $K_{s,O}$

457   is $10^{-41.8}$ for goethite and 10^{-39} for ferrihydrite (see Table VII-13, p. 228 in Lemire et al., 2013;

458   Stefánsson, 2007). This indicates that goethite has a slightly lower solubility compared to

459   ferrihydrite, and therefore should precipitate first if the kinetic rate allows it. Applied to the

460   experiment sid02 (pH 1.6, 500 ppm $As^{(V)}$, see Table 1), the concentration of $Fe^{(III)}$ next to the

461   siderite surface is high enough to precipitate goethite. This implies that locally the solubility of

462   $Fe^{(III)}$ is above the equilibrium value at this pH, $K=2.5\cdot10^{-2}$ mol·m^{-3}. Under these conditions, the

463   rate of siderite dissolution measured from the AFM experiments is of the order of $R =10^{-7}$

464   mol·m^{-2}·s^{-1} (see Section 3.1). We now consider a simplified system where $Fe^{(III)}$ is produced at

465   a rate R above the siderite surface and diffuses perpendicular to it with a length scale $L_{diff} =$

466   $\sqrt{Dt}$, where D is the diffusion coefficient of water, of the order of $2\cdot10^{-9}$ m^2·s^{-1}, and t is time.

467 Then, one can define the characteristic thickness $L_b = \frac{KD}{R}$ of a thin boundary layer in which the

468 iron concentration is higher than K in our experiments. Using the values given above for K, D,

469 and R, one obtains L_b=250 micrometers. This simple scaling relationship indicates that the fluid

470 above siderite can remain supersaturated with respect to iron at distance orders of magnitude

471 larger than the height of the oxyhydroxide precipitates observed to form, as long as siderite

472 continues to dissolve. In this boundary layer, the pH will be buffered by the release of carbonate

473 groups from the siderite that will increase locally the pH and therefore will reduce the value of

474 K, increasing even more the supersaturation with respect to goethite. Such variations of fluid

475 pH at mineral surfaces during dissolution have been reported using phase-shift interferometry

476 (Ruiz-Agudo et al., 2016).

477 A more complex model would take into account the rate of $Fe^{(II)}$ oxidation, the rate of

478 precipitation of iron oxyhydroxides, the speciation of iron species, and the buffering of pH in

479 the boundary layer, but would not change the conclusion that a thin layer with specific

480 thermodynamic properties is present above the siderite crystal and act as a micro-reactor for the

481 precipitation of iron oxyhydroxide particles. Another implication is that this local increase of

482 pH would favor adsorption of arsenic onto the newly formed iron oxyhydroxide particles.

483 We also observed that, after some time, oxyhydroxide particles were attached to the surface and

484 were not removed by the AFM tip during the scanning. They must have had some form of

485 bonding at the surface and therefore the underlying siderite structure must have been involved

486 in that attachment, in addition to the boundary layer effect.

487 To summarize, there is a clear control of the siderite surface on the precipitation of iron

488 oxyhydroxide particles. This control is mainly due to the presence of a fluid boundary layer

489 where iron will be more concentrated in the fluid near the siderite surface, and where the

490 dissolution rate exceeds diffusion of ionic species away from the dissolving surface. This is

similar to observations reported for the precipitation of arsenic or selenium phases on calcite (Putnis et al., 2013; Renard et al., 2015).

4.3 Adsorption of arsenic

The interactions of arsenic with minerals and solutions represent an important environmental issue, and several natural systems show both high arsenic concentration and low fluid pH, such as acid mine or borehole fluid drainage (Benner et al., 1999; Norstrom et al., 2000) and remediation is a key challenge (Mohan and Pittman, 2007). We discuss here how arsenic interacts with siderite and iron oxyhydroxides in our experiments. The two main observations are that 1) arsenic adsorbs mainly on iron oxyhydroxides and a little, if any, on siderite, 2) the presence of high arsenic concentration in the fluid does not significantly modify the mechanism nor the rate of the coupled dissolution-precipitation process.

Jönsson and Sherman (2008) have studied the sorption of arsenic on synthetic iron carbonates and found that at pH above 7, siderite strongly adsorbs arsenic, whereas at lower pH, it was not possible to measure this adsorption due to the production of iron oxides. Conversely, the adsorption capacity of iron oxides can reach 20 milligrams of arsenic adsorbed per gram of dry iron oxide, with values usually less than 5 mg/g in most sets of laboratory experiments (Badruzzaman et al., 2004; Westerhoff et al., 2005; Mohan and Pittman, 2007).

The strong adsorption of arsenic in various oxidation states ($As^{(III)}$ and $As^{(V)}$) on iron oxides, such as amorphous goethite and magnetite, has been measured by Dixit et al. (2003) in solutions in a range of pH between 4 and 10. The amount of adsorbed arsenate (As^V) and arsenite (As^{III}) on ferrihydrite varies slightly with pH in the range 3-11, with trends of increasing adsorption for arsenite and decreasing adsorption for arsenate as pH increases in the range 2.5-9 (Raven et al., 1998; Dixit and Hering, 2003). Above pH ~9, arsenite adsorption on iron oxyhydroxide decreases as well (see Fig. 7 in Raven et al., 1998).

515   Arsenate tetrahedra adsorb onto ferrihydrite iron oxides by linking an edge with Fe octahedra,

516   based on EXAFS measurements of the distance between $Fe^{(III)}$ and $As^{(V)}$ atoms (Manceau,

517   1995). This adsorption also retards the growth of iron particles and slows down the rate of

518   transformation of ferrihydrite to hematite. It is controlled by the surface charge and density of

519   sorption sites on iron oxides that both vary with pH and fluid composition (Goldberg and

520   Johnson, 2001; Dixit and Hering, 2003).

521   In our experiments we observe that the presence of arsenic does not significantly change the

522   mechanism of siderite dissolution, nor the precipitation of iron oxyhydroxides: the pattern of

523   dissolution and the morphology of precipitates is independent of the presence or absence of

524   arsenic. When iron oxyhydroxides precipitate, however, the adsorption of arsenic onto these

525   minerals is expected, as has been demonstrated in a previous study (Dixit et al., 2003). Our situ

526   observations indicate that the continuous production of iron oxyhydroxide due to the dissolution

527   of siderite will create new adsorption sites for arsenic on the one hand, but on the other hand

528   these particles of oxyhydroxides cover the surface of siderite and may passivate it in less than

529   a day at pH below 2.

530

531   **5. Conclusion**

532   The coupled process of siderite dissolution in acidic aqueous fluids, in the presence of arsenic,

533   was studied in-situ using atomic force microscopy (Figure 8). The main results are:

534   - Dissolution of siderite occurs by the nucleation of etch pits and step edge retreat, as observed

535   previously (Duckworth and Martin, 2004; Tang and Martin, 2011), and by a third mechanism

536   identified here, the widening and deepening of cleavage planes.

537   - Coupled to siderite dissolution, iron oxyhydroxide precipitates as nanometer size particles on

538   the surface (heterogeneous nucleation) and primary nanoparticles are then self-assembled into

539   rounded aggregates that coalesce to form larger particle aggregates, probably amorphous, 130-

540   220 nm wide and up to 80 nm high that cover the carbonate surface. This process reduces the

541   surface area available for dissolution and may passivate the siderite surface. Goethite and a

542   weak Raman peak at the position of ferrihydrite were identified from flow-through reactor

543   experiments.

544   - The presence of arsenic, even at high concentration, does not significantly modify the siderite

545   dissolution process. Arsenic preferentially adsorbs onto the iron oxyhydroxide precipitates

546   formed from the interface-coupled dissolution and precipitation process occurring under acidic

547   aqueous conditions, typically occurring in acid mine drainage environments.

548

558

559   **References**

560   Abou-Hassan, A., Sandre, O., Neveu, S., Cubuil, V., 2009. Synthesis of goethite by separation

561   of the nucleation and growth processes of ferrihydrite nanoparticles using microfluidics.

562   Angewandte Chemie 121, 2378-2381.

563   Badruzzaman, M., Westerhoff, P., Knappe, D. R., 2004. Intraparticle diffusion and adsorption

564   of arsenate onto granular ferric hydroxide (GFH). Wat. Res. 38(18), 4002-4012.

565   Benner, S. G., Blowes, D. W., Gould, W. D., Herbert, R. B., Ptacek, C. J., 1999. Geochemistry

566   of a permeable reactive barrier for metals and acid mine drainage. Env. Sci. & Tech. 33(16),

567   2793–2799.

568   Beverskog, B., Puigdomenech, I. 1996. Revised Pourbaix diagrams for iron at 25–300 C.

569   Corrosion Science 38(12), 2121-2135.

570   Bruno, J., Wersin, P., Stumm, W., 1992. On the influence of carbonate in mineral dissolution:

571   II. The solubility of $FeCO_3$ (s) at 25° C and 1 atm total pressure. Geochim. Cosmochim. Acta

572   56(3), 1149–1155.

573   Byelov, D. V., Meijer, J.-M., Snigireva, I., Snigirev, A., Rossi, L., van der Pol, E., Kuijk, A.,

574   Philipse, A., Imhof, A., van Blauderen, A., Vroege, G. J., Petukhov, A. V., 2013. In situ hard

575   X-ray microscopy of self-assembly in colloidal suspensions. RSC Adv. 3, 15670-15677.

576   Chapman, E. C., Capo, R. C., Stewart, B. W., Hedin, R. S., Weaver, T. J., Edenborn, H. M.

577   2013. Strontium isotope quantification of siderite, brine and acid mine drainage contributions

578   to abandoned gas well discharges in the Appalachian Plateau. Appl. Geochem. 31, 109–118.

579   Cornell, R. M., & Schwertmann, U. 2003. The iron oxides: structure, properties, reactions,

580   occurrences and uses. John Wiley & Sons.

581   Davison, W., & Seed, G. 1983. The kinetics of the oxidation of ferrous iron in synthetic and

582   natural waters. Geochimica et Cosmochimica Acta 47(1), 67-79.

583   Dixit, S., Hering, J. G., 2003. Comparison of arsenic (V) and arsenic (III) sorption onto iron

584   oxide minerals: implications for arsenic mobility. Env. Sci. & Tech. 37 (18), 4182–4189.

585   Duckworth, O. W., Martin, S. T., 2004. Role of molecular oxygen in the dissolution of siderite

586   and rhodochrosite. Geochim. Cosmochim. Acta 68 (3), 607–621.

587   Gebauer, D., Völkel, A., Cölfen, H., 2008. Stable prenucleation calcium carbonate clusters.

588   Science 322 (5909), 1819–1822.

589   Goldberg, S., Johnston, C. T., 2001. Mechanisms of arsenic adsorption on amorphous oxides

590   evaluated using macroscopic measurements, vibrational spectroscopy and surface

591   complexation modelling. J. Colloid & Interface Sci. 234, 204-216.

592   Golubev, S. V., Bénézeth, P., Schott, J., Dandurand, J. L., Castillo, A., 2009. Siderite

593   dissolution kinetics in acidic aqueous solutions from 25 to 100 C and 0 to 50 atm pCO_2. Chem.

594   Geol. 265 (1), 13–19.

595   Guo, H., Stüben, D., Berner, Z., 2007a. Adsorption of arsenic (III) and arsenic (V) from

596   groundwater using natural siderite as the adsorbent. J. Colloid & Interface Sci. 315 (1), 47–53.

597   Guo, H., Stüben, D., Berner, Z., 2007b. Arsenic removal from water using natural iron mineral–

598   quartz sand columns. Sci. Tot. Env. 377 (2), 142–151.

599 Hanesch, M., 2009. Raman spectroscopy of iron oxides and (oxy)hydroxides at low laser power

600 and possible applications in environmental magnetic studies. Geophys. J. Int. 177, 941-948.

601 Hedin, R. S., Stafford, S. L., Weaver, T. J., 2005. Acid mine drainage flowing from abandoned

602 gas wells. Mine Water and the Environment 24 (2), 104–106.

603 Jönsson, J., Sherman, D. M., 2008. Sorption of As (III) and As (V) to siderite, green rust

604 (fougerite) and magnetite: Implications for arsenic release in anoxic groundwaters. Chem. Geol.

605 255 (1), 173–181.

606 Lemire, R.J., Berner, U., Musikas, C., Palmer, D.A., Taylor, P., Tochiyama, O., 2013. Chemical

607 Thermodynamics of Iron, Part 1. NEA No. 6355. OECD. https://www.oecd-

608 nea.org/dbtdb/pubs/6355-vol13a-iron.pdf

609 Lin, Y. B., Lin, Y. P., Liu, C. W. , Tan, Y. C., 2006. Mapping of spatial multi-scale sources of

610 arsenic variation in groundwater on ChiaNan floodplain of Taiwan. Sci. Tot. Env. 370 (1), 168–

611 181.

612 Liu, H., Li, P., Zhu, M., Wei, Y., Sun, Y. 2007. Fe (II)-induced transformation from ferrihydrite

613 to lepidocrocite and goethite. Journal of Solid State Chemistry 180(7), 2121-2128.

614 Lu, P., Zhu, C. 2011. Arsenic Eh–pH diagrams at 25 C and 1 bar. Environmental Earth Sciences

615 62(8), 1673-1683.

616 Manceau, A., 1995. The mechanism of anion adsorption on iron oxides: Evidence for the

617 bonding of arsenate tetrahedra on free Fe (O, OH) 6 edges. Geochim. Cosmochim. Acta 59(17),

618 3647-3653.

619   Milliken, K. L., 1998. Carbonate diagenesis in non-marine foreland sandstones at the western

620   edge of the Alleghanian overthrust belt, southern Appalachians. In: Carbonate Cementation in

621   Sandstones: Distribution Patterns and Geochemical Evolution, Special Publication 26 of the

622   International Association of Sedimentologists, pp 64–87.

623   Mohan, D., Pittman, C. U., 2007. Arsenic removal from water/wastewater using adsorbents—

624   a critical review. J. Hazard. Mat. 142(1), 1-53.

625   Montes-Hernandez, G., Renard, F., Findling, N., Auzende A-L., 2015. Formation of porous

626   calcite mesocrystals from CO_2-H_2O-$Ca(OH)_2$ slurry in the presence of common domestic

627   drinks. CrystEngComm 17, 5725-5733.

628   Morad, S., Ismail, H. B., Ros, L. D., Al-Aasm I. S., Serrhini, N. E., 1994. Diagenesis and

629   formation water chemistry of Triassic reservoir sandstones from southern Tunisia.

630   Sedimentology 41 (6), 1253–1272.

631   Nordstrom, D. K., Alpers, C. N., Ptacek, C. J., & Blowes, D. W., 2000. Negative pH and

632   extremely acidic mine waters from Iron Mountain, California. Env. Sci. & Tech. 34(2), 254-

633   258.

634   Pal, T., Mukherjee, P. K., Sengupta, S., Bhattacharyya, A. K., Shome, S., 2002. Arsenic

635   pollution in groundwater of West Bengal, India - An insight into the problem by subsurface

636   sediment analysis. Gondwana Research 5 (2), 501–512.

637   Parkhurst, D. L., Appelo, C. A. J., 1999. Users guide to PHREEQC (version 2) A computer

638   program for speciation, batch reaction, one dimensional transport and inverse geochemical

639   calculations, Water-Resources Investigation report 99-4259, U.S. Geological Survey:

640   Washington, DC, p. 312.

641 Putnis, C. V., Renard, F., King, H., Montes-Hernandez, G., Ruiz-Agudo, E., 2013.

642 Sequestration of selenium on calcite surfaces revealed by nanoscale imaging. Env. Sci. & Tech.

643 47, 13469–13476.

644 Raven, K. P., Jain, A., Loeppert, R. H., 1998. Arsenite and arsenate adsorption on ferrihydrite:

645 kinetics, equilibrium, and adsorption envelopes. Env. Sci. & Tech. 32(3), 344-349.

646 Reiterer, F., Johannes, W., Gamsjäger, H., 1981. Semimicro determination of solubility

647 constants: copper (II) carbonate and iron (II) carbonate. Microchimica Acta 75 (1–2), 63–72.

648 Renard, F., Putnis, C. V., Montes-Hernandez, G., Ruiz-Agudo, E., Hovelmann, J., Sarret, G.,

649 2015. Interactions of arsenic with calcite surfaces revealed by in-situ nanoscale imaging.

650 Geochim. Cosmochim. Acta 159, 61–79.

651 Rossi, C., Marfil, R., Ramseyer, K., Permanyer, A., 2001. Facies-related diagenesis and

652 multiphase siderite cementation and dissolution in the reservoir sandstones of the Khatatba

653 Formation, Egypt's Western Desert. J. Sed. Res. 71 (3), 459–472.

654 Ruiz-Agudo E., Kowacz M., Putnis C. V., Putnis A., 2010. The role of background electrolytes

655 on the kinetics and mechanism of calcite dissolution. Geochim. Cosmochim. Acta 74, 1256–

656 1267.

657 Ruiz-Agudo, E., Putnis, C. V., 2012. Direct observations of mineral-fluid reactions using

658 atomic force microscopy: the specific example of calcite. Min. Mag. 76, 227–253.

659 Ruiz-Agudo, C., Ruiz-Agudo, E., Putnis, C. V., Putnis, A., 2015. Mechanistic principles of

660 barite formation: from nanoparticles to micron-sized crystals. Crystal Growth & Design 15 (8),

661 3724–3733.

662   Ruiz-Agudo, E., King, H. E., Patiño-López, L. D., Putnis, C. V., Geisler, T., Rodriguez-
663   Navarro, C., Putnis, A. 2016. Control of silicate weathering by interface-coupled dissolution-
664   precipitation processes at the mineral-solution interface. Geology 44(7), 567-570.

665   Schwertmann, U., Murad, E. 1983. Effect of pH on the formation of goethite and hematite from
666   ferrihydrite. Clays and Clay Minerals 31(4), 277-284.

667   Singer, P. C., Stumm, W., 1970. The solubility of ferrous iron in carbonate-bearing waters. J.
668   Am. Water Works Assoc. 62 (3), 198–202.

669   Stefánsson, A. 2007. Iron (III) hydrolysis and solubility at 25 C. Environmental science &
670   technology 41(17), 6117-6123.

671   Stel, H., 2009. Diagenetic crystallization and oxidation of siderite in red bed (Buntsandstein)
672   sediments from the Central Iberian Chain, Spain. Sedim. Geol. 213 (3), 89–96.

673   Tang, Y., Martin, S. T., 2011. Siderite dissolution in the presence of chromate. Geochim.
674   Cosmochim. Acta 75 (17), 4951–4962.

675   Teng, H. H., 2013. How ions and molecules organize to form crystals. Elements 9 (3), 189–
676   194.

677   Walter, A. L., Frind, E. O., Blowes, D. W., Ptacek, C. J., Molson, J. W., 1994. Modeling of
678   multicomponent reactive transport in groundwater: 1. model development and evaluation.
679   Water Resources Research 30 (11), 3137–3148.

680   Wang, Y., Reardon, E. J., 2001. A siderite/limestone reactor to remove arsenic and cadmium
681   from wastewaters. Appl. Geochem. 16 (9), 1241–1249.

682   Weidler, P. G., Hug, S. J., Wetche, T. P., Hiemstra, T. 1998. Determination of growth rates of

683   (100) and (110) faces of synthetic goethite by scanning force microscopy. Geochimica et

684   Cosmochimica Acta 62(21), 3407-3412.

685   Westerhoff, P., Highfield, D., Badruzzaman, M., Yoon, Y., 2005. Rapid small-scale column

686   tests for arsenate removal in iron oxide packed bed columns. J. Envir. Eng., 131(2), 262-271.
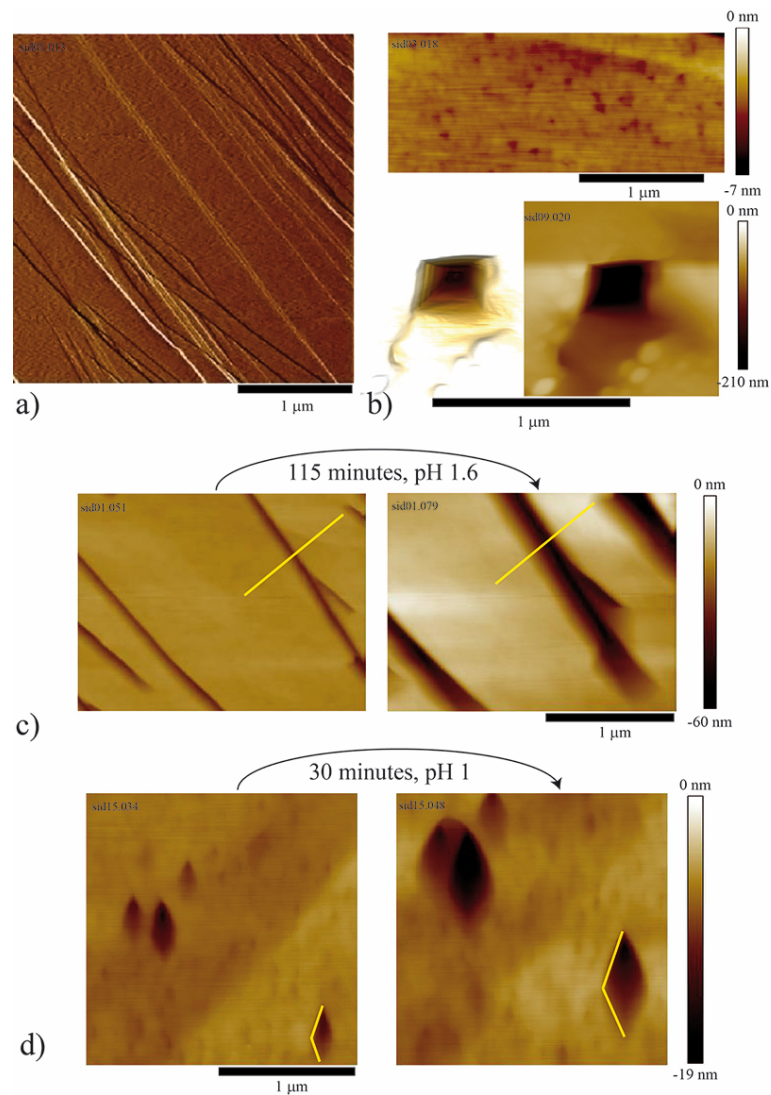
Figures

Figure 1: In-situ AFM images of a siderite surface. a) Dry cleaved surface showing steps (image in deflection mode). Siderite steps are mostly one unit cell, 4.72Å high. b) Rhombohedral etch pits forming on the siderite surface during dissolution in a flow-through fluid cell. Top (height mode): one unit cell deep etch pits start developing. Bottom (3D view, left, and height mode right): 210 nm deep 4-sided etch pit. c) Dissolution occurs also by widening and deepening of cleavage steps (exp. sid09, As$^{(V)}$ 500 ppm, pH 2.1, see Table 1). The yellow line corresponds to the time-lapse height profiles shown on Figure 2. d) Dissolution along etch pits and etch pit merging. The dissolution rate can be measured through the length increase of etch pit sides (yellow lines).

698
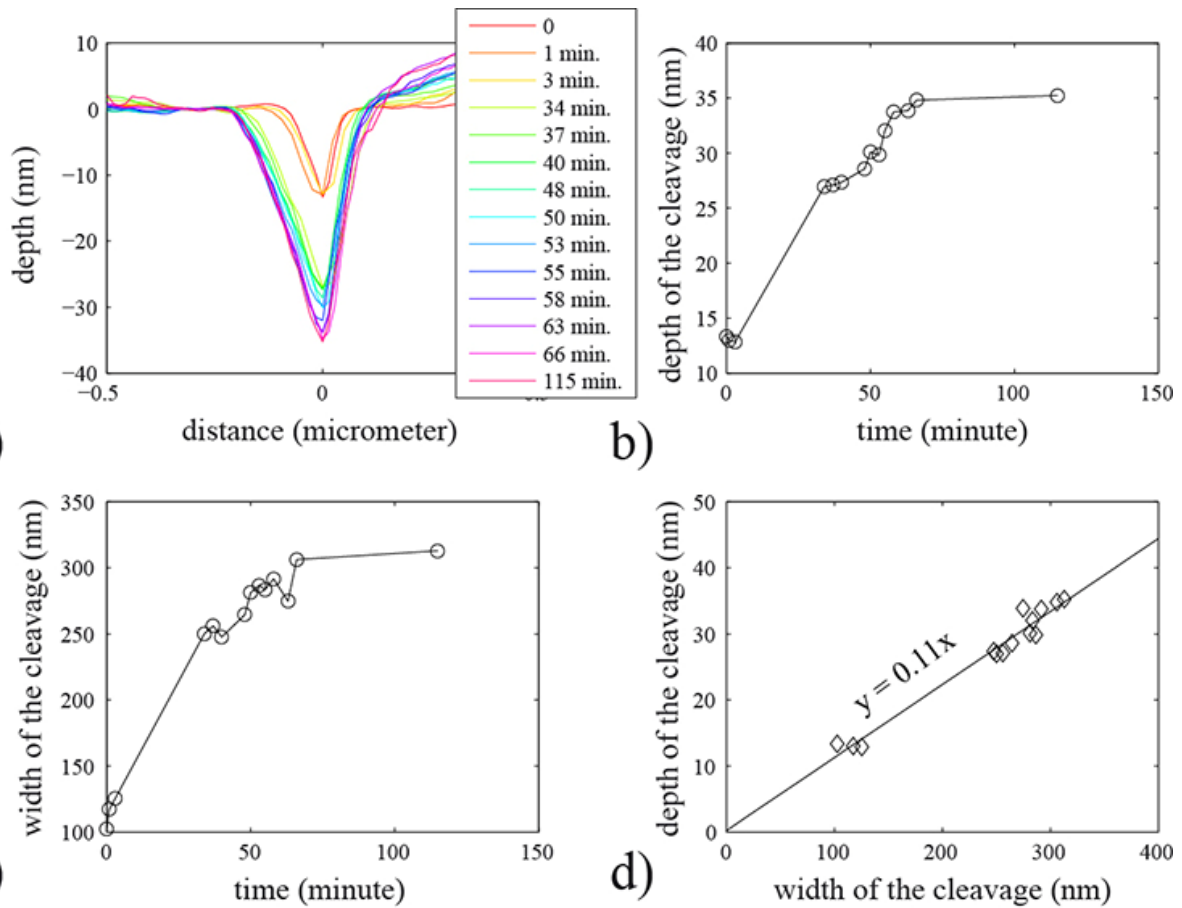
**Figure 2**: Dissolution along a siderite surface (exp. sid09, As$^{(V)}$ 500 ppm, pH 2.1, see Table 1), where a cleavage step deepens and widens with time. a) Time-lapse profiles perpendicular to the cleaved (10-14) surface (the profile is shown on Figure 1c). b) Depth as a function of time. c) Width as a function of time. d) Depth as a function of width showing a linear relationship and indicating dissolution perpendicular to the interface that preserves the wedge geometry of the cleavage.

705
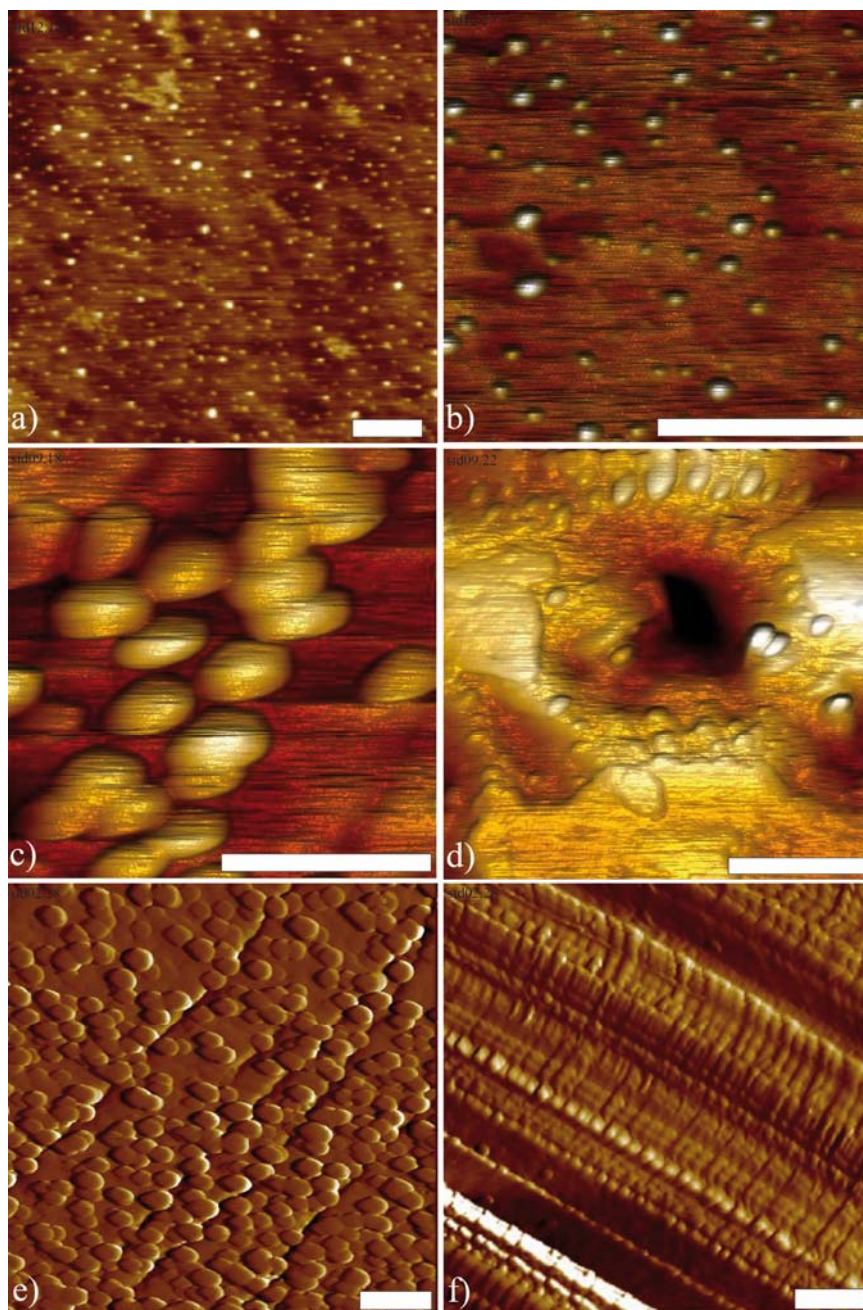
Figure 3: AFM images of iron oxide/hydroxide precipitates on a siderite surface. Scale bar: 500 nm for all images. a-b) Small iron oxyhydroxide particles randomly precipitated on the siderite surface (height mode, exp. sid12, no arsenic, pH 2.8, see Table 1); c-d) Iron oxyhydroxide precipitates, with an etch pit showing evidence of dissolution (d) coupled to precipitation (height mode, exp. sid09, As$^{(V)}$ 500 ppm, pH 2.1, see Table 1). e-f) Iron oxide/hydroxide particles aligned along steps of the siderite surface (deflection mode, exp. sid02, As$^{(V)}$ 500 ppm, pH 1.6, see Table 1).
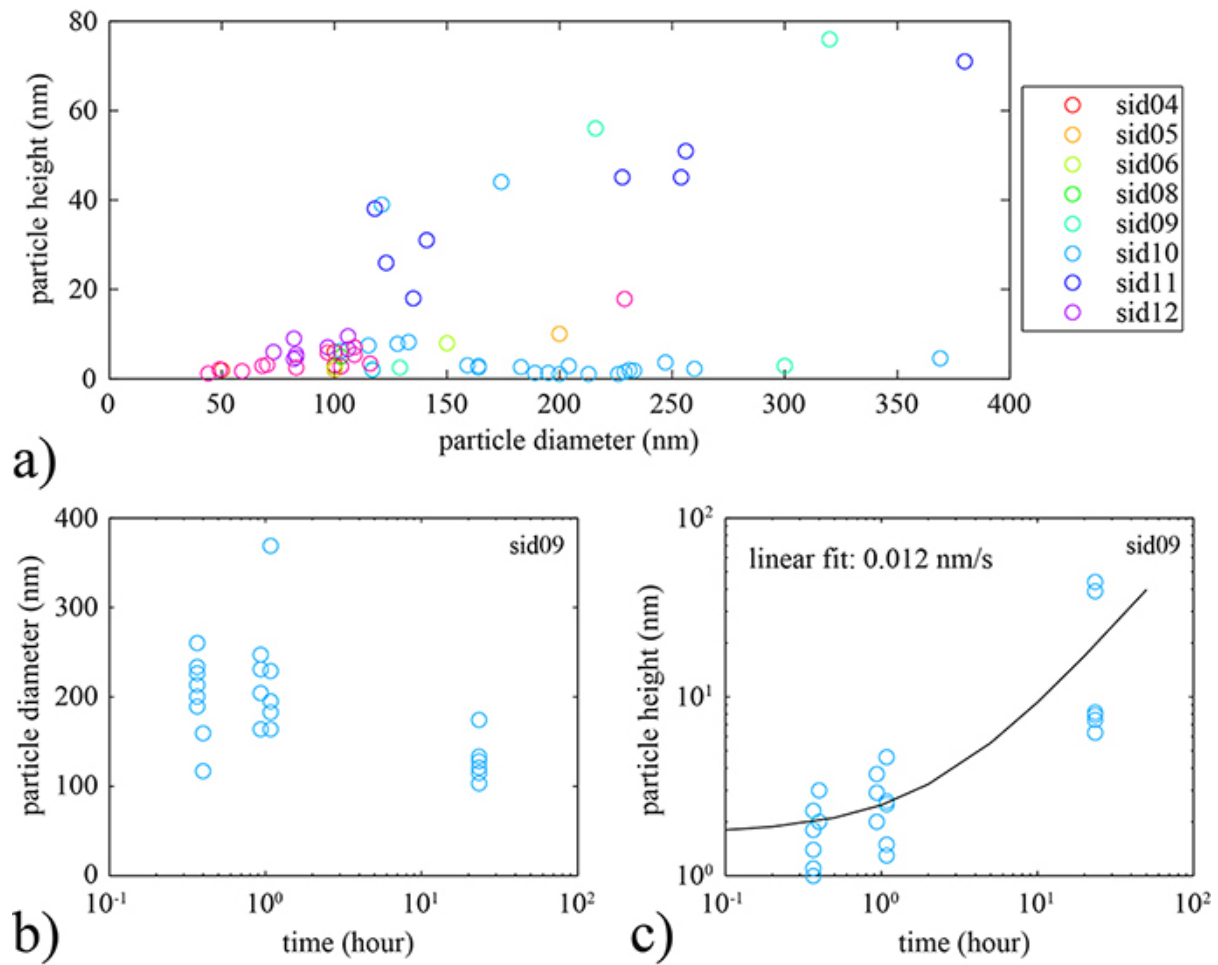
Figure 4: Analysis of the shape of the iron oxyhydroxide particles precipitated on siderite surfaces. a) Particle height versus diameter. b-c) For experiment sid09 (As$^{(V)}$ 500 ppm, pH 2.1, see Table 1), the evolution of the particle diameter (c) and height (d) as a function of time is shown. The average particle diameter does not change significantly with time whereas the height of iron oxyhydroxide particle tends to increase with time (best linear fit is given).
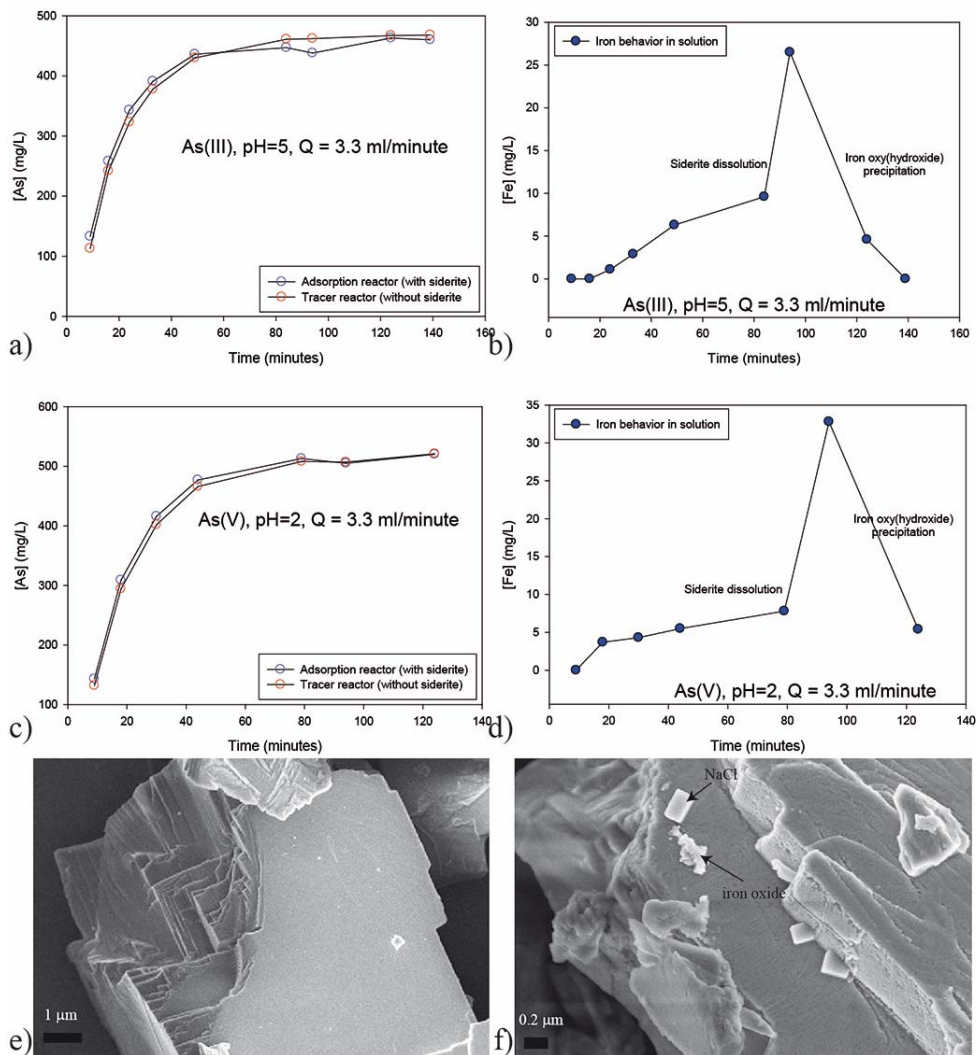
Figure 5: Results of stirred flow-through reactor experiments and field emission scanning electron microscopy image of siderite crystals and precipitates of iron oxyhydroxide. a-b) Siderite at pH 5 with As[(III)] 500 ppm (exp. Ba1, see Table 1): no adsorption of As could be detected (a), whereas the time evolution of iron concentration in the fluid shows an initial increase (siderite dissolution) and a drop after around 100 minutes (iron oxyhydroxide precipitation). c-d) Same as a-b) for a solution at pH 2 and As[(V)] 500 ppm (exp. Ba2, see Table 1). e-f) Field emission scanning electron microscopy image of an unreacted siderite grain used for the stirred flow-through reactor experiments (e) and siderite grain after reaction showing small iron oxyhydroxide precipitates and NaCl crystals (f). NaCl is an evaporation product after the conclusion of the experiments.

730
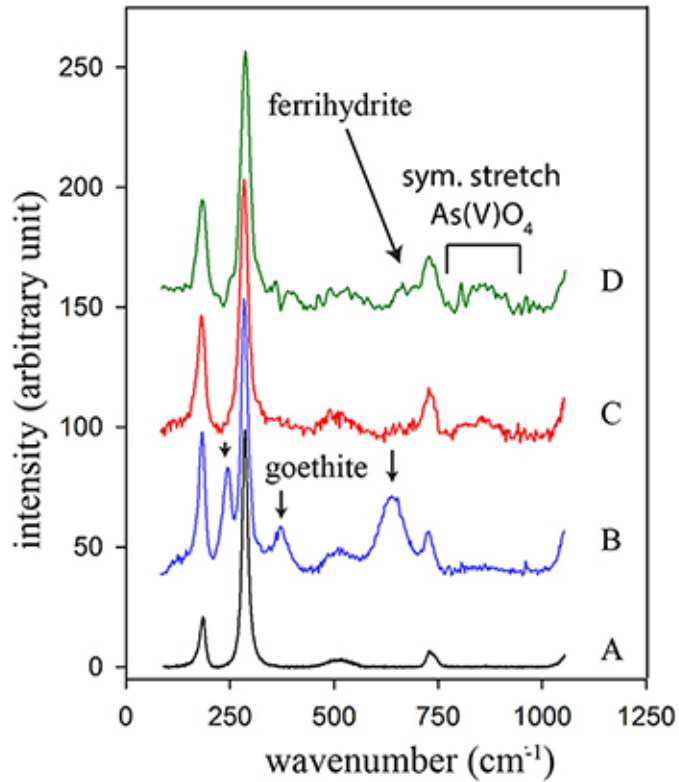
Figure 6: Raman spectra showing original siderite (black, A), precipitates from the pH 2 flow-through reactor experiment without (blue, B) and with (red, C) the peak at 857 cm^{-1} characteristic of arsenate symmetrical stretching vibration and precipitate from the reactor experiment at pH 5 (green, D). Peaks of goethite are clearly visible in sample B (black arrows), and a weak peak at the position of ferrihydrite could also be observed on sample D.

736
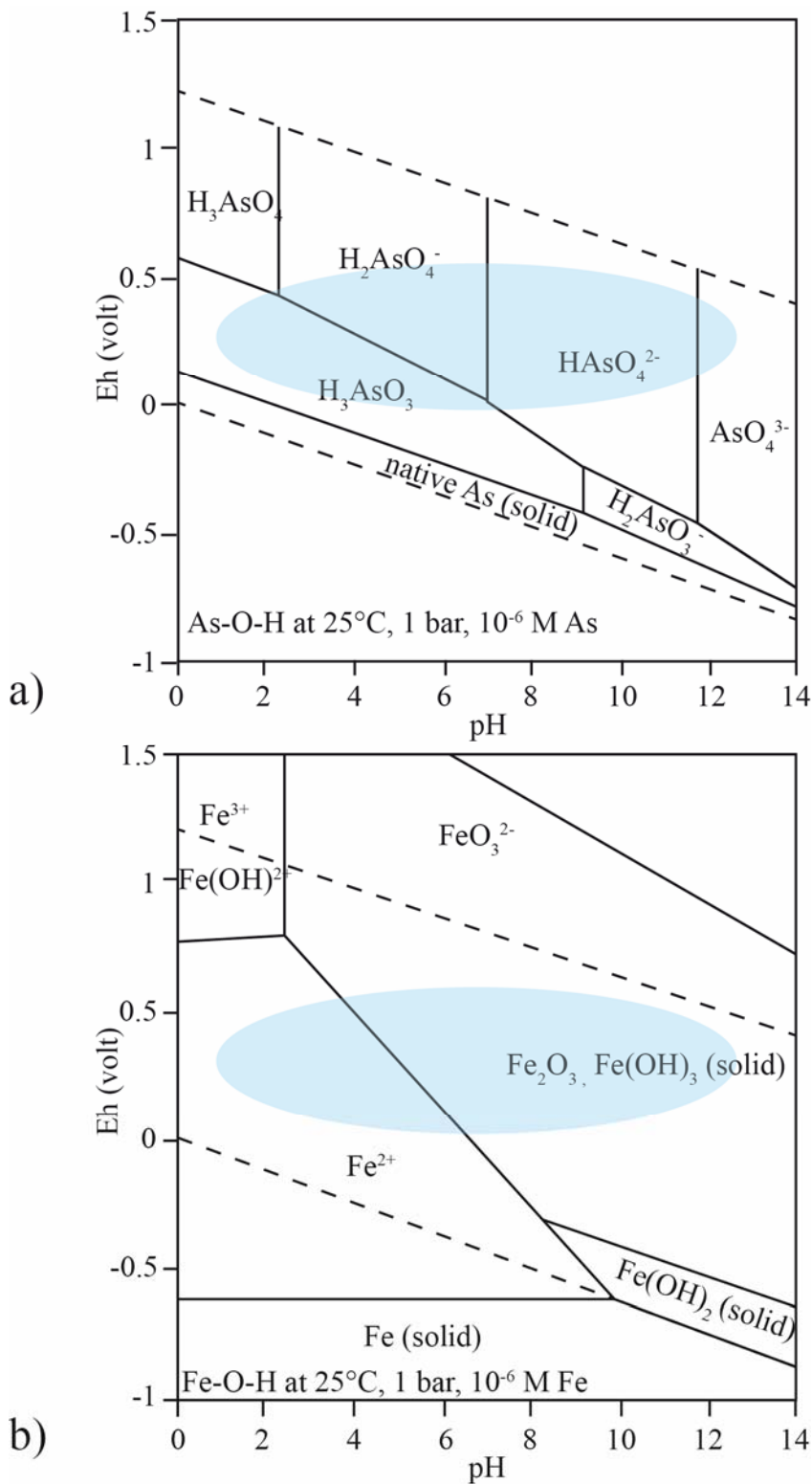
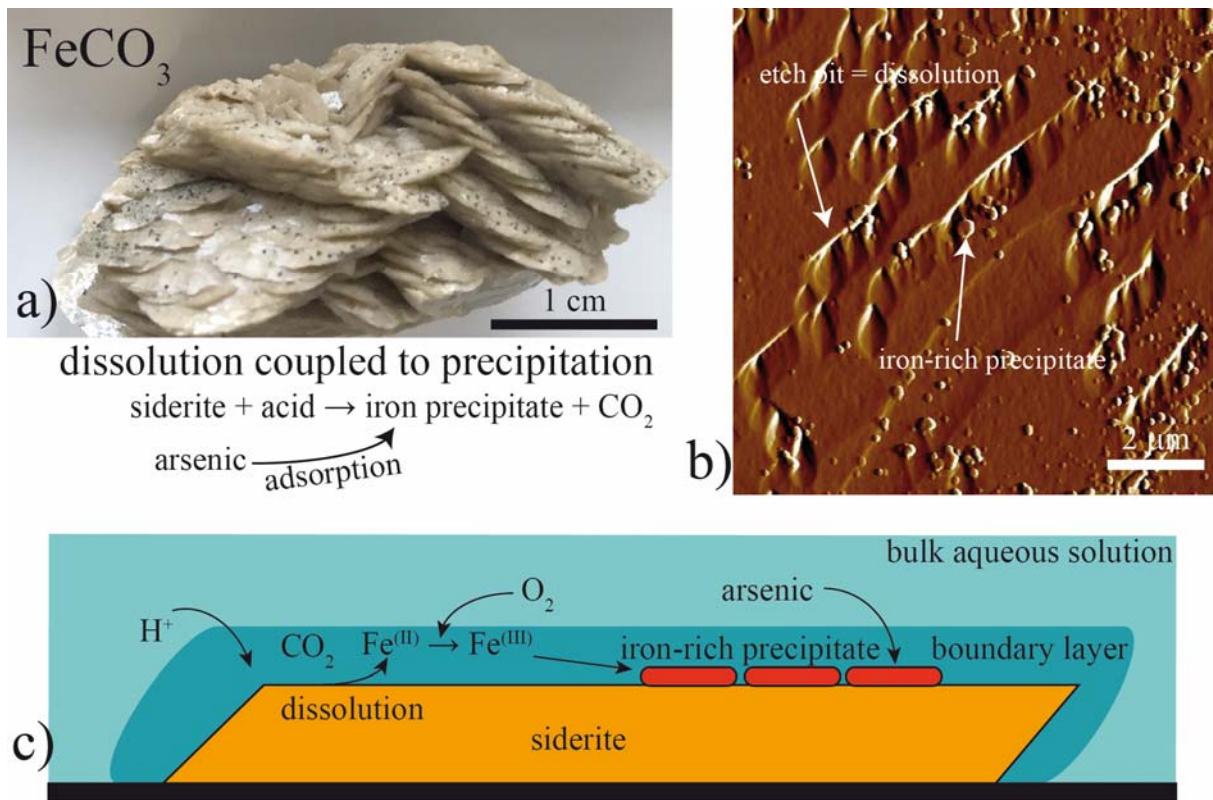**Figure 7**: Pourbaix diagrams for a) iron (Beverskog and Puigdomenech, 1996) and b) arsenic (Lu and Zhu, 2011) at 25°C and 1 bar in the water system. The conditions of the AFM and flow-through reactor experiments are underlined by the shaded ellipse.

Figure 8: Summary of the coupled process of siderite dissolution, iron oxyhydroxide precipitation, and arsenic adsorption. a) Natural siderite sample used for the AFM experiments. The sample was crushed and clean siderite millimeter-size and freshly cleaved crystals were used. b) AFM image of a siderite crystal surface in deflection mode, showing both etch pits (rhombohedral shapes) and iron oxyhydroxide precipitates (circular shapes). c) Sketch of the coupled dissolution-precipitation process.

749   **Table 1**: List of in-situ atomic force microscopy (AFM) and stirred flow-through reactor

750   experimental conditions for coupled siderite dissolution and iron oxyhydroxide precipitation in

751   the presence of arsenic. The pH is that of the injected solution.

Exp. #	Ionic strength (mole/l)	Duration (hour)	Arsenic concentration	pH measured	Precipitates (surface area covered)
AFM					
sid01	0.047	5.2	0	5.5	
			$As^{(V)}$, 50 ppm	1.3	<5%
			$As^{(V)}$, 500 ppm	1.6	<5%
sid02	0.047	21.9	$As^{(V)}$, 500 ppm	1.6	>80%
sid03	0.047	3.5	0	5.5	
			$As^{(V)}$, 50 ppm	1.3	< 5%
			$As^{(V)}$, 500 ppm	1.6	<5%
sid04	0.047	24	0	5.5	
			$As^{(V)}$, 500 ppm	4.7	>80%
sid05	0.047	21	0	5.5	
			$As^{(III)}$, 500 ppm	4.7	>80%
sid06	0.047	28.5	0	5.5	
			$As^{(III)}$, 500 ppm	1.6	<10%
sid07	0.047	2.2	0	5.4	
			$As^{(V)}$, 500 ppm	2.8	no precipitates after 2h
sid08	0.047	24.9	0	5.5	
			$As^{(V)}$, 500 ppm	1.7	<5%
sid09	0.047	23.5	0	5.5	
			$As^{(V)}$, 500 ppm	2.1	>80%

sid10	0.047	24	0	5.5	<20%, precipitates aligned along steps
sid11	0.047	17	0	1.6	>80%
sid12	0.047	17	0	2.8	<10%
sid13	0.047	1.2	As$^{(III)}$, 500 ppm	11.7	no precipitates
sid14	0.047	1	As$^{(V)}$, 500 ppm	12.1	no precipitates
sid15	0.047	8.7	0	2	<10%
				1	>80%
sid16	0.047	0.8	0	2	<10%
				1	>80%
Reactor					
Ba1	0.047	2.3	As$^{(III)}$, 500 ppm	5	-
Ba2	0.047	2.3	As$^{(V)}$, 500 ppm	2	-

752